Applied Energy 329 (2023) 120211

Contents lists available at ScienceDirect

Applied Energy

journal homepage: www.elsevier.com/locate/apenergy

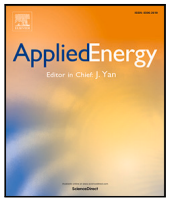

High-temperature heat recovery from a solar reactor for the thermochemical redox splitting of H_2O and CO_2

Alon Lidor *, Yves Aschwanden, Jamina Häseli, Pit Reckinger, Philipp Haueter, Aldo Steinfeld

Department of Mechanical and Process Engineering, ETH Zurich, 8092, Zurich, Switzerland

ARTICLE INFO

Keywords:
Solar fuels
Heat recovery
Solar reactor
High-temperature heat recovery

ABSTRACT

The solar splitting of H_2O and CO_2 via a thermochemical redox cycle offers a viable pathway for producing sustainable drop-in fuels for the transportation sectors. The key performance metric is its solar-to-fuel energy efficiency, which is strongly dependent on the ability to recover heat during the temperature swing between the reduction and oxidation steps. Here we report on the experimental investigation of a novel heat recovery method based on coupling the solar reactor with two thermocline energy storage units made of a packed-bed of alumina spheres. Using N_2 as an inert heat transfer fluid, the heat rejected during cooling from the reduction to the oxidation temperature is stored and, following the oxidation step, delivered back to preheat the solar reactor towards the reduction temperature, thus reducing the required solar input and consequently increasing the efficiency. With a first experimental prototype, a heat extraction effectiveness of up to 70% from a 4 kW solar reactor is obtained with measured N_2 outlet temperatures exceeding 1250°C. Energy flow modeling of a 50 kW solar reactor predicts a theoretical upper limit value of the energy efficiency of 42% for perfect heat recovery without transient losses, and 14.7% with such losses included. Several improvements and insights into high-temperature heat recovery are detailed.

1. Introduction

Long-haul aviation and maritime sectors are strongly dependent on liquid transportation fuels. The production of drop-in fuels from H_2O and CO_2 using solar energy can eliminate greenhouse gas emissions derived from fossil fuels and contribute to making transportation more sustainable. A promising pathway is via the thermochemical redox cycle for splitting H_2O and CO_2, driven by concentrated sunlight [1]. The product is a specific mixture of H_2 and CO – syngas – which can be further processed downstream to liquid transportation fuels by established gas-to-liquid synthesis (e.g. Fischer–Tropsch). The entire process chain to kerosene and methanol has been successfully demonstrated in concentrating solar dish and solar tower configurations using a solar reactor containing a reticulated porous ceramic (RPC) structure made of ceria [2,3]. The 2-step redox cycle based on ceria is represented by:

Reduction:

$$\frac{1}{\Delta\delta}CeO_{2-\delta_{ox}} -> \frac{1}{\Delta\delta}CeO_{2-\delta_{red}} + \frac{1}{2}O_2, \quad (1)$$

oxidation with CO_2:

$$\frac{1}{\Delta\delta}CeO_{2-\delta_{red}} + CO_2 -> \frac{1}{\Delta\delta}CeO_{2-\delta_{ox}} + CO, \quad (2)$$

and oxidation with H_2O:

$$\frac{1}{\Delta\delta}CeO_{2-\delta_{red}} + H_2O -> \frac{1}{\Delta\delta}CeO_{2-\delta_{ox}} + H_2. \quad (3)$$

$\Delta\delta = \delta_{red} - \delta_{ox}$ denotes the redox extent. The redox cycle can be operated under a temperature-swing mode and/or a pressure-swing mode to control $\Delta\delta$ and thereby the fuel yield per cycle. For typical operating conditions of the reduction step at 1500 °C and 0.1 mbar and the oxidation step at 900 °C and 1 bar, thermodynamics predicts $\Delta\delta = 0.04$ [2]. The key performance metric of the solar reactor is the solar-to-fuel energy efficiency $\eta_{solar\text{-}to\text{-}fuel}$, defined as the ratio of the heating value of the syngas produced to the sum of the solar energy input Q_{solar} and any parasitic energy inputs such as those associated with vacuum pumping and/or inert gas consumption. Since the reduction extent increases at lower oxygen partial pressures, the use of an inert sweep gas or a vacuum pump is required to have a reasonable O_2 release from the ceria. A vacuum pump was found to be superior in performance and to have a smaller energy penalty compared to the inert sweep gas method [4–6]. To date, the maximum experimentally obtained $\eta_{solar\text{-}to\text{-}fuel}$ is 5.25% with a 4 $kW_{thermal}$ solar reactor [4] and 5.6% with a 50 $kW_{thermal}$ solar reactor [7], both solar reactors performing the CO_2 splitting redox cycle without any heat recovery. The relatively

* Corresponding author.
E-mail address: alidor@ethz.ch (A. Lidor).

https://doi.org/10.1016/j.apenergy.2022.120211
Received 3 August 2022; Received in revised form 14 October 2022; Accepted 22 October 2022
Available online 16 November 2022

Nomenclature

Roman symbols

c_p	Specific heat capacity, $\mathrm{J\,kg^{-1}\,K^{-1}}$
e_i	Specific energy of term i, $\mathrm{kJ/mol_{CeO_2}}$
f_losses	Heat losses fraction from HT piping
m_Ce	Ceria mass, kg
$\dot{m}_\mathrm{HTF}$	Heat transfer fluid flow rate, $\mathrm{kg\,s^{-1}}$
p_reactor	Reactor pressure, bar
P_solar	Solar power, kW
Q_ch	TES charge energy, kJ
Q_dis	TES discharge energy, kJ
Q_extract	Extracted heat, kJ
Q_fuel	Fuel energy, kJ
Q_inert	Inert gas separation energy, kJ
Q_other	Other heat losses, kJ
Q_pump	Pumping energy, kJ
Q_recover	Recovered heat, kJ
Q_rerad	Re-radiation losses, kJ
$Q_\mathrm{RPC,s}$	RPC sensible energy, kJ
Q_solar	Solar energy, kJ
T_amb	Ambient temperature, °C
$T_\mathrm{heat\ extraction}$	Maximum heat extraction temperature, °C
$t_\mathrm{heat\ extraction}$	Heat extraction duration, min
T_HR	RPC temperature at the end of the heat recovery
$T_\mathrm{ox,end}$	Oxidation end temperature, °C
$T_\mathrm{ox,start}$	Oxidation start temperature, °C
T_red	Reduction end temperature, °C
$\dot{V}$	Volumetric flow rate, $\mathrm{L\,min^{-1}}$

Greek symbols

$\Delta\delta$	Redox extent
δ_ox	Oxidation nonstoichiometry extent
δ_red	Reduction nonstoichiometry extent
$\varepsilon_\mathrm{heat\ extraction}$	Heat extraction effectiveness
$\varepsilon_\mathrm{heat\ recovery}$	Heat recovery effectiveness
$\eta_\mathrm{solar\text{-}to\text{-}fuel}$	Solar to fuel energy efficiency
$\eta_\mathrm{solar\text{-}to\text{-}fuel,max}$	Maximum solar-to-fuel energy efficiency
η_TES	TES energy storage efficiency

Abbreviations

DHS	Dual heat storage
HFSS	High flux solar simulator
HS	High temperature side
HTF	Heat transfer fluid
HTV	High-temperature valve
LS	Low temperature side
RPC	Reticulated porous ceramics
TES	Thermal energy storage

low value obtained for $\eta_\mathrm{solar\text{-}to\text{-}fuel}$ is mainly due to the sensible heat of the RPC rejected during the temperature-swing redox cycling, which represented about 43% of Q_solar [7]. Recovering most of it can in principle boost $\eta_\mathrm{solar\text{-}to\text{-}fuel}$ to values exceeding 20% [8–10].

Heat recovery concepts included counter-rotating rings with non-volatile redox material mounted on them, incorporating solid–solid heat recovery [11], but involved moving components at ultra-high temperatures which can become troublesome for long-term operation [12]. A similar concept consisted of using two concentric cylinders that counter-rotate [13]. A 3D heat transfer analysis predicted a heat recovery effectiveness of over 50%, and solar-to-fuel energy efficiency of up to 5% [14]. However, no experimental data is available for validation. A generic model [15] for a counter-current solid redox material based on solid–solid heat recovery through radiation between reduced and oxidized elements predicted heat exchanger efficiency of 80%, a reactor efficiency of 22% for an idealized case and 16% for a case with practical assumptions on energy requirements. A particular concept of a counter-current setup consisted of moving bricks for physically separating the reduction, oxidation, and heat recovery steps into different chambers [16]. A thermodynamic analysis predicted a heat exchanger efficiency of 80%, and an increase in the solar-to-chemical efficiency by a factor of 3, up to values of 25%. No experimental data is available for this concept either.

High-temperature heat recovery using inert heat transfer particles that recover heat from the reduced redox particles avoids recombination reactions that can occur when performing direct heat recovery between reduced and oxidized particles [17]. Modeling six consecutive heat recovery stages predicted a heat recovery rate of over 70% at optimized conditions. Characterization of the heat transfer between two particle species in a packed bed at 250 °C revealed that the heat transfer coefficient increases with increasing mean temperature and decreasing contact time [18]. However, the transport of particles at 1500 °C is challenging. Heat recuperation using liquid metal as a heat transfer fluid (HTF) enables decoupling the solar receiver from the redox reactor [19]. Modeling an array of solar receivers and reaction chambers predicted a thermal-to-chemical energy efficiency of 19.8% for the case of ceria as a redox material, and heat recuperation effectiveness of 80%.

A numerical model for the heat recovery and storage using gas as a heat transfer medium in a closed loop system with a single thermal energy storage (TES) unit predicted a decrease of up to 40% in the required solar energy input for a theoretical 300 kW solar reactor [20]. During an experimental testing of a 250 kW sweep gas operated solar reactor, heat exchangers for gas–gas heat recovery were included in the setup [21]. However, no heat recovery performance was reported. The concept of high-temperature heat recovery using two thermocline-based TES units each coupled with an indirectly chemically reactive zone and a separate solar receiver has been previously developed [22]. With this arrangement, the heat rejected from one reactive zone during cooling from reduction to oxidation temperature is recovered and stored in the adjacent TES unit. Following oxidation, the heat stored is delivered back to preheat the reactive zone towards the reduction temperature, thus reducing the required solar input and consequently increasing $\eta_\mathrm{solar\text{-}to\text{-}fuel}$. The first proof-of-concept was realized using electrical heaters instead of a solar receiver and air as the indirect HTF [22]. While the heat recovery step was demonstrated, it was done after an initial preheating of 38 h, thus starting from a steady-state temperature distribution that is not characteristic for real solar reactors operating in short cycles.

While different concepts for solar redox reactors incorporating heat recovery have been theoretically studied, experimental data is only available for the counter-current rings concept [12]. An isothermal redox cycle was demonstrated experimentally with ceria [23] and hercynite [24] but thermodynamic analyses indicated low efficiencies and conversion extents [23,24]. As such, the experimental development and demonstration of a high-temperature heat recovery is critical.

In this work, we present a new high-temperature heat recovery method, based on the dual storage system, dubbed as the dual heat storage (DHS) system. The main novelty is the use of a solar reactor in lieu of a solar receiver, and using two TES units without reactive zones. The DHS thus allows for a directly irradiated RPC, avoiding the heat losses incurred by an indirect design, but at the expense of using an inert HTF due to direct heat exchange between the RPC and the HTF during heat recovery. The design also requires performing the

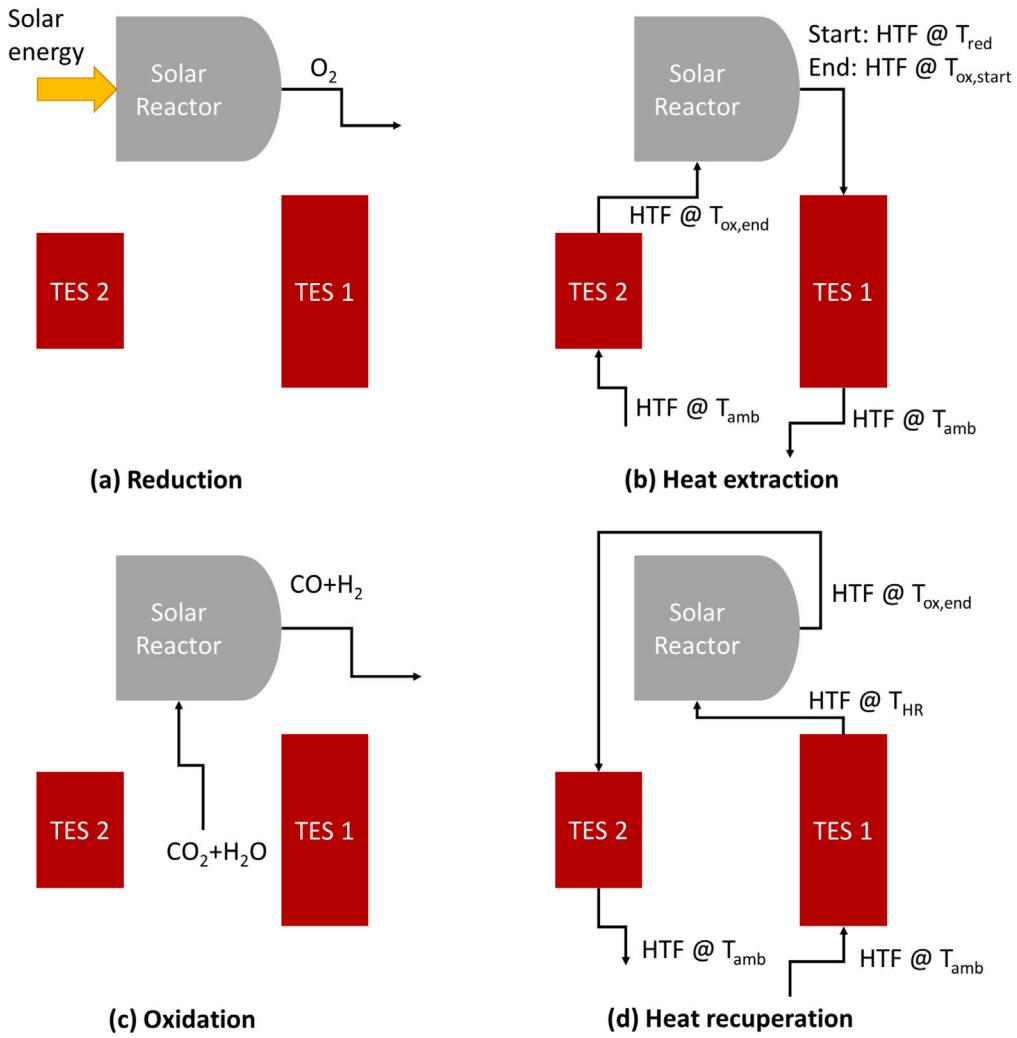

Fig. 1. The four cycle steps of the DHS system: (a) reduction, in which the solar reactor receives a solar radiative power input and is operated under vacuum, releasing O_2 from the RPC; (b) heat extraction, in which the HTF flows through TES 2 into the solar reactor, extracting heat and charging TES 1; (c) oxidation, in which the reactants (CO_2 in our case) flow into the reactor, re-oxidizing the RPC and the product stream (CO) flows out; (d) heat recuperation, in which the HTF flows through TES 1, discharging it, and heats the solar reactor from $T_{ox,end}$ to the maximum heat recovery temperature T_{HR} and then flows from the solar reactor via TES 2, recovering the residual HTF heat.

flow control between reactor and TES units, at high temperatures. The setup was experimentally tested at the ETH's high-flux solar simulator (HFSS) to mimic the heat transfer characteristics and operational field conditions of solar concentrating systems.

2. The dual heat storage (DHS) system

The DHS system consists of the solar redox reactor, similar in design to the previous solar reactors with RPC [4], and two TES units. Instead of the two steps cycle, reduction and oxidation, the new cycle consists of four steps: reduction, heat extraction, oxidation, and heat recuperation as schematically described in Fig. 1. During the reduction step, the solar reactor is irradiated by the HFSS and heated up to a desired reduction temperature, T_{red} (max. 1500 °C). At the same time, a vacuum is pulled inside the solar reactor to reduce the oxygen partial pressure while a relatively small argon flow is injected next to the window to protect it from ceria dust. The evolved O_2 exits the reactor cavity and flows through a gas analysis unit. Once T_{red} is attained, the solar input supplied via the HFSS is stopped and the heat extraction step begins. An HTF flows first through the small TES unit (TES 2) - where it is heated from ambient temperature T_{amb} to the oxidation temperature –, enters the solar reactor via the main inlet port – where it is further heated by the RPC to the reduction temperature –, exits through the outlet rear port and enters the large TES unit (TES 1) – where it is finally cooled to T_{amb}. During this step, the solar reactor cools down to a desired temperature for the start of the oxidation step, $T_{ox,start}$. Since the nominal temperature of the solar reactor's outlet ideally varies from T_{red} to $T_{ox,start}$, the maximum stored temperature at TES 1, T_{HR}, will be somewhat lower than T_{red}. Furthermore, since it is critical that no oxygen is introduced into the solar reactor to avoid unwanted premature re-oxidation of the RPC, an inert HTF (in our case N_2) must be used during the heat extraction phase. In the subsequent oxidation step, the gaseous reactants H_2O and/or CO_2 are fed into the reactor, re-oxidizing the ceria and generating syngas. Even though this reaction is exothermic, the reactor temperature slowly decreases due to conduction heat losses through the shell and re-radiation through the aperture. At the end of the oxidation, the reactor is at its lowest temperature, $T_{ox,end}$. The last heat recuperation step commences by reversing the HTF flow through TES 1, extracting the high temperature heat stored there and transferring it into the solar reactor. The HTF exits the solar reactor at roughly $T_{ox,end}$, passes through TES 2 and finally exits. In this manner, TES 2 stores the HTF's heat between T_{amb} and $T_{ox,end}$. Once the solar reactor reaches the outlet temperature from TES 1, no more heat can be recovered into the reactor, and the heat recuperation is stopped. At this point, the cycle is completed and a new cycle begins with the reduction step. With this combined heat storage

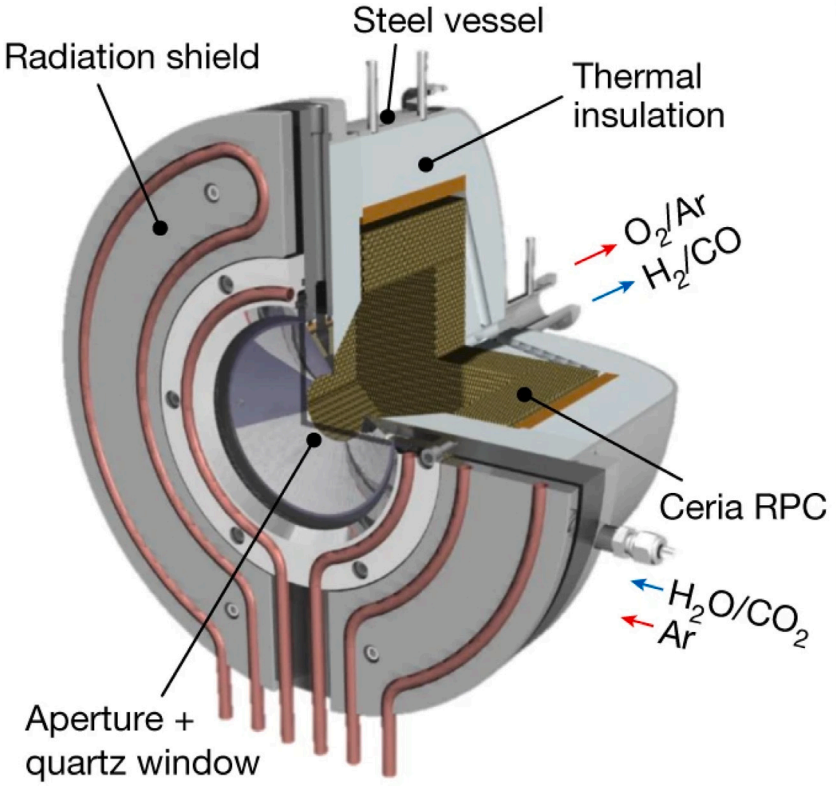

Fig. 2. Scheme of the solar reactor design: frontal aperture with quartz window, aluminum radiation shield with cooling water tubes, gas inlet/outlet, ceria RPC, alumina–silica thermal insulation, and stainless steel vessel. The red arrows indicate the flows during reduction: the blue arrows during oxidation. Reproduced from [2].

and exchange scheme, the required solar energy input is decreased and, consequently, the $\eta_{\text{solar-to-fuel}}$ is increased.

While each step in the cycle flows through the solar reactor, separation is required between the two loops, namely the redox-loop and the TES-loop. The redox-loop includes the solar reactor, vacuum pump, and gas analysis unit, and is active during the reduction and oxidation steps. The TES-loop includes the solar reactor and both TES units, and is active during the heat extraction and heat recuperation steps. The redox-loop is operated under vacuum pressures during reduction and at slightly above ambient pressure during oxidation. The TES-loop operates at above ambient pressure due to the higher flow rates of the HTF across both TES units. Flow control is implemented by four high-temperature valves (HTV), made of stainless steel housing and a carbon rotating disc, capable of operating both under vacuum and positive pressures.

3. Experimental setup

3.1. Solar reactor

The design of the solar reactor, shown schematically in Fig. 2, has been described in detail previously [2,4]; we highlight here its most important features. It consists of an octagonal cavity lined by a high-temperature Al_2O_3–SiO_2 insulation (Altraform KVS 184/400 by Rath) and enclosed by a cylindrical outer shell made of stainless steel. The cavity contains the RPC structure made of eight side bricks and a backplate, forming an inner cavity of roughly 100 mm diameter and 75 mm depth. The RPC bricks are 35 mm thick, with a total mass of 2788 g, feature dual-scale porosity in the mm and μm range, and are manufactured by the replication method [25]. The reactor has a 40 mm aperture at the front which is sealed by a 4 mm-thick clear fused quartz window for the access of concentrated solar radiation. Thus, with this arrangement, the RPC structure is directly exposed to the high-flux radiation, providing volumetric absorption and effective heat transfer to the reaction site [4].

Table 1
TES specifications.

	Units	TES1	TES2
Storage medium mass	kg	4.258	2.214
Length	m	0.7	0.35
Diameter	m	0.1	
Sphere diameter	mm	3–5	
Sphere density	kg m^{-3}	997–1277	
Solid volume fraction		0.6811	0.7083

3.2. Thermal energy storage units

The schematic of the TES units is presented in Fig. 3. The two TES units differ in size but their design is identical. Each unit consists of an external stainless steel body, composed of three parts: a cylindrical shell, a high temperature side (HS) flange on top, and a low-temperature side (LS) flange at the bottom. The insulation consists of an external microporous insulation (Promalight 1000 by Promat) and an internal fibrous insulation (Altraform KVS 184/400 by Rath). The storage section consists of an alumina pipe filled with porous alumina spheres (Activated Alumina GP by Comelt). The details of the packed bed of both TES units are provided in Table 1. The bottom of the storage section is supported by a steel diffuser plate, while at the HS flange a diffuser is machined inside the high-temperature fibrous insulation. At the bottom part of the LS flange, there is an opening for the insertion of the thermocouples into the packed bed, while side nozzles allow for thermocouples placement in the insulation and outside the storage section.

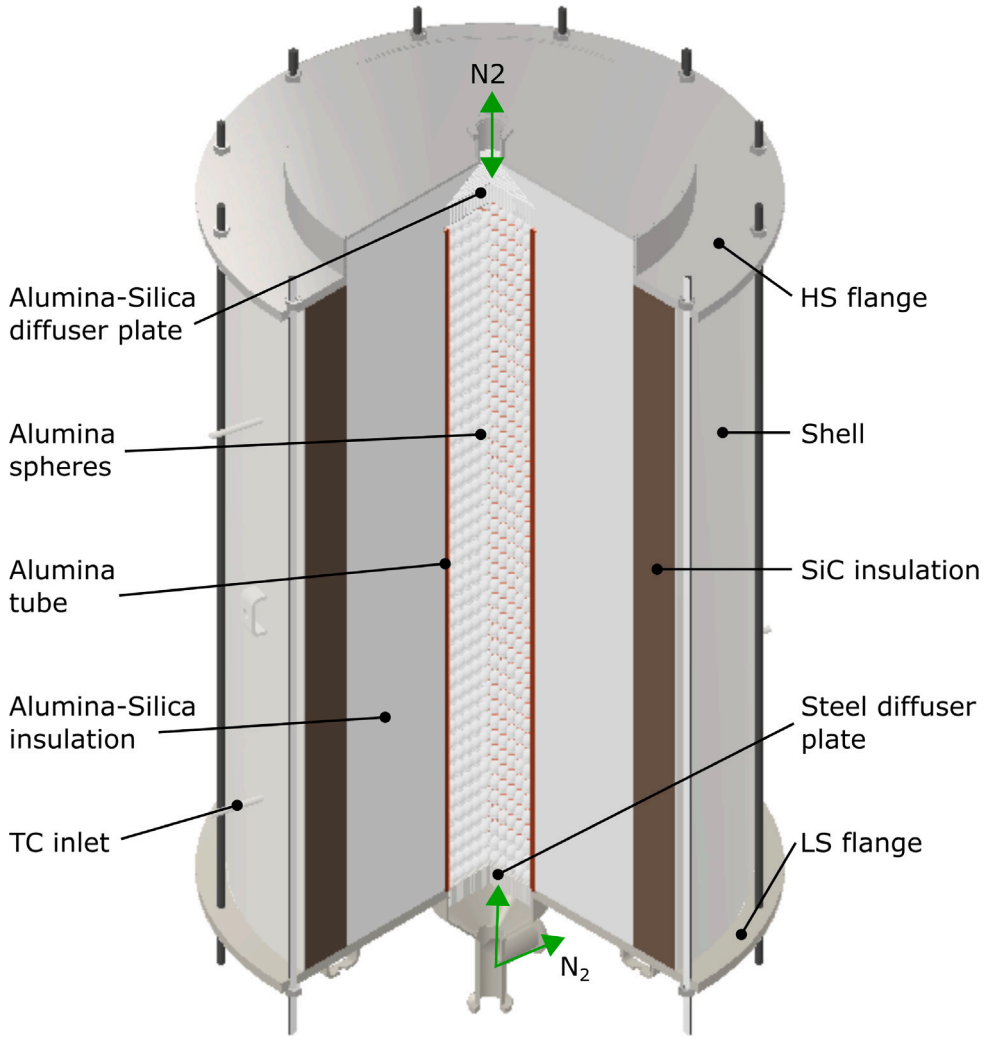

Fig. 3. Scheme of the TES design: stainless steel shell, alumina–silica insulation and diffuser plate, microporous SiC insulation, alumina pipe, alumina spheres (storage section), steel diffuser plate, and the HS and LS flanges. The N_2 flow direction is from top to bottom during charging and from bottom to top during discharging.

3.3. Control and measurement system

The process scheme of the DHS system with the solar reactor subsystem and the TES subsystem is depicted in Fig. 4. The experiments were performed at the ETH's HFSS, comprised of an array of seven high-pressure Xenon arcs. The solar thermal radiative power P_{solar} was measured before the experiments using a water-cooled calorimeter with an identical aperture and front section as the solar reactor. The RPC temperature was measured using 4 B-type thermocouples, and their average is denoted the nominal reactor temperature $T_{reactor}$. The outlet flow from the reactor was measured with an additional B-type thermocouple. Several K-type thermocouples were used to measure the temperatures of the external reactor shell, water cooling system, vacuum pump inlet, and TES insulation. The packed-bed temperature in TES 1 was measured by 14 thermocouples (10 B-type and 4 K-type), placed at 7 different locations along the symmetry axis, with one thermocouple at the center of the packed bed and one at the internal side of the alumina pipe wall at each height (see Fig. 5). In addition, K-type thermocouples were placed at the inlet of each TES unit. The different flows (Ar, N_2, CO_2) were controlled by 4 mass flow controllers (Bronkhorst), and the vacuum pressure during reduction was achieved by a dry vacuum pump (Pfeiffer Vacuum ACP 15). Two pressure sensors were installed directly connected to the reactor cavity (Keller) and the vacuum pump inlet (Gems Sensors). The composition of the product gas streams during reduction and oxidation was analyzed by IR detectors for CO and CO_2 and electrochemical sensor for the O_2 (Siemens Ultramat 23). The flows were controlled by four custom-designed HTVs, which are suitable for high temperatures and for both positive pressure and vacuum operation. The high- and intermediate-temperature piping was made of stainless steel piping components with an internal alumina pipe and a layer of Al_2O_3–SiO_2 insulation between the pipes. An external layer of stone–wool insulation (Flumroc FMI 500) was added outside the steel pipe to reduce heat losses.

3.4. Performance indicators

Several performance indicators were used in the analysis of the DHS operation. The solar-to-fuel energy efficiency is defined as:

$$\eta_{\text{solar-to-fuel}} = \frac{Q_{\text{fuel}}}{Q_{\text{solar}} + Q_{\text{pump}} + Q_{\text{inert}}}, \tag{4}$$

where Q_{fuel} is the energy value of the generated fuel, Q_{solar} is the total solar energy input ($Q_{\text{solar}} = \int P_{\text{solar}} dt$), Q_{pump} is the pumping energy requirement (of both vacuum during reduction and HTF pumping during heat extraction and heat recovery), and Q_{inert} is the energy required for inert gas separation. The values for the auxiliary terms Q_{pump} and Q_{inert} are converted from work to heat in accordance with the norm [26]. The energy storage efficiency of the TES units is given by [27]

$$\eta_{\text{TES}} = \frac{Q_{\text{dis}}}{Q_{\text{ch}}}, \tag{5}$$

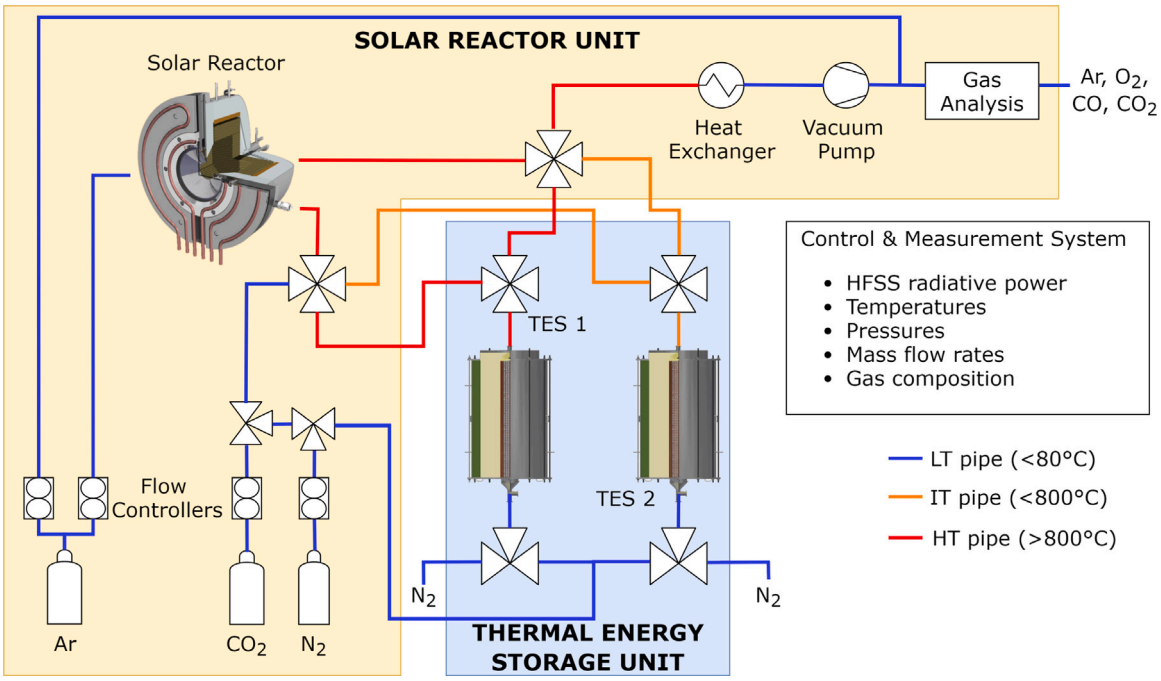

Fig. 4. Process scheme of the DHS system. The solar reactor subsystem includes the solar reactor, gas supply, mass flow controllers, valves, 2 HTVs, heat exchanger, vacuum pump, and gas analysis unit. The TES subsystem consists of the two TES units, 2 HTVs, and the valves at the bottom of the TES units. The piping system is grouped into high temperature (HT, red), intermediate temperature (IT, orange), and low temperature (LT, blue) lines.

in which the numerator denotes the total energy discharged from the TES and the denominator denotes the sum of the energy charged into the TES. Unlike a standard standalone TES unit, the required HTF pumping energy is already considered in Eq. (4) and hence is not repeated here. The heat extraction effectiveness is defined as the ratio between the heat transferred to the HTF during the heat extraction step over the amount of sensible heat extracted from the RPC and the various energy losses during heat extraction:

$$\varepsilon_{\text{heat extraction}} = \frac{Q_{\text{extract}}}{Q_{\text{RPC,s}} + Q_{\text{other}}} = \frac{\dot{m}_{\text{HTF}} \int \left(h_{\text{out}} - h_{\text{in}}\right) dt}{m_{\text{Ce}} \int_{T_{\text{ox,start}}}^{T_{\text{red}}} c_{p,\text{Ce}} dT_{\text{Ce}} + Q_{\text{other}}}. \quad (6)$$

The other losses (Q_{other}) comprise of the re-radiation from the aperture, convective and radiative losses from the shell to the ambient, heat transferred from the insulation to the HTF, and heat lost to the cooling water. The heat recovery effectiveness is defined as the ratio of the heat transferred to the RPC during heat recuperation step over the required sensible heating of the RPC from $T_{\text{ox,end}}$ to T_{red}:

$$\varepsilon_{\text{heat recovery}} = \frac{Q_{\text{recover}}}{Q_{\text{RPC,s}}} = \frac{m_{\text{Ce}} \int_{T_{\text{ox,end}}}^{T_{\text{HR}}} c_{p,\text{Ce}} dT_{\text{Ce}}}{m_{\text{Ce}} \int_{T_{\text{ox,end}}}^{T_{\text{red}}} c_{p,\text{Ce}} dT_{\text{Ce}}}. \quad (7)$$

A thermodynamic analysis for the DHS system has been performed using the specific energy terms normalized to the amount of ceria in moles (such as in [9]). e_{fuel} is the specific fuel energy, e_{solar} is the specific required solar energy input, e_{inert} is the specific inert gas separation energy, and e_{pump} is the specific required pumping energy. The sum of energy input is denoted as $e_{\text{total}} = e_{\text{solar}} + e_{\text{inert}} + e_{\text{pump}}$ [26] and the term e_{solar} equals to

$$e_{\text{solar}} = e_{\text{RPC,s,HR}} + e_{\text{red}} + e_{\text{transient}} + e_{\text{rerad}} \quad (8)$$

with $e_{\text{RPC,s,HR}}$ as the specific sensible RPC heating energy (modified by the extent of $\varepsilon_{\text{heat recovery}}$), e_{red} is the specific reduction energy, $e_{\text{transient}}$ is the transient heating and cooling losses term, and e_{rerad} denotes the specific re-radiation losses (see S.I. for details). The other performance indicators such as the CO_2 conversion extent X_{CO_2} or selectivity are not affected by the heat recovery system and are defined identically to previous works [4,26]. The uncertainties in gas compositions, flow rates, and temperatures were estimated by propagating the measurement errors of the different instruments as provided by manufacturers specifications (see S.I.).

4. Experimental results

All experiments were performed for $P_{\text{solar}} = 4.2$ kW, supplied by 6 arcs of the HFSS. During the reduction step, $p_{\text{reactor}} = 20$ mbar−22 mbar, $\dot{V}_{\text{Ar}} = 0.5$ L min^{-1}, $T_{\text{red}} = 1450$ °C − 1500 °C. During oxidation step, $\dot{V}_{CO_2} = 7$ L min^{-1}, $T_{\text{ox,start}} = 900$ °C, $T_{\text{ox,end}} = 650$ °C − 750 °C.

A reference run of 3 consecutive CO_2-splitting cycles without applying the DHS system, i.e. only reduction and oxidation steps but skipping the heat extraction and heat recuperation steps, is presented in Fig. 6 for the purpose of comparison with those runs with the DHS system. Plotted are the temporal variation of the nominal solar reactor temperature T_{reactor}, p_{reactor}, and specific O_2 and CO evolution rates, r_{O_2} and r_{CO}. For this run, $\eta_{\text{solar-to-fuel}} = 3.3\%$ because no heat was actually recovered and no attempt was undertaken to optimize the solar reactor design and operation for the present study.

A representative run of 3 consecutive CO_2-splitting cycles of the DHS system is presented in Fig. 7. Only 3 steps were applied in this run: reduction, heat extraction, and oxidation, because the charging temperature into the TES 1 unit was too low (< $T_{\text{ox,end}}$) to allow for a heat recuperation step. Plotted are the temporal variations of T_{reactor}, p_{reactor}, and r_{O_2} and r_{CO}, as well as the fluid temperature at the reactor outlet T_{outlet} (N_2 during heat extraction, CO and CO_2 during oxidation), the HTF temperature at the TES HS side (inlet during heat extraction), $T_{\text{TES,HS}}$, and the packed bed temperature $T_{\text{TES,C1}}$ (upper TC).

The use of four HTVs and multiple connecting pipes resulted in larger pressure drops, resulting in $p_{\text{reactor}} = 55$ mbar during reduction, compared to 22 mbar for the standard redox cycles of Fig. 6. As a result, the O_2 release rate was smaller, leading to a 22% lower reduction extent and, consequently, a lower CO yield. In addition, some of the CO was

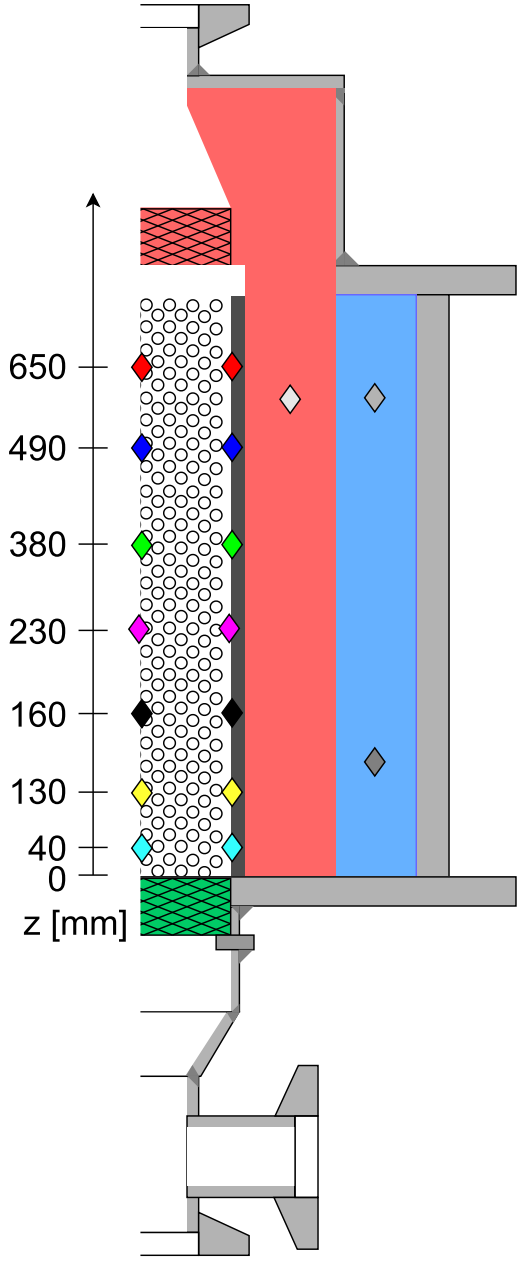

Fig. 5. Location of the thermocouples in TES 1. The thermocouples in the packed bed are inserted from the bottom, with a pair at each height (center and wall). The thermocouples in the insulation are inserted radially via orifices in the shell.

Table 2
Summary of the results for DHS testing.

Parameter	Units	Values
$t_{\text{heat extraction}}$	min	5.5–9.6
$T_{\text{heat extraction}}$	°C	1162–1267
$\epsilon_{\text{heat extraction}}$	%	49.53–69.81
$\eta_{\text{solar-to-fuel}}$	%	1.52–2.44
$\eta_{\text{solar-to-fuel,max}}$	%	1.64–2.83
f_{losses}	%	78.3–82.4

presumably converted to CO_2 due to the Boudouard reaction in the HT piping, as evidenced by solid carbon depositions.

During the heat extraction step p_{reactor} was slightly above 2 bar at a N_2 flow of 90 L min^{-1}, limiting the flow rate of the HTF used. However, the pressure gradients across the RPC and TES were $\Delta p_{\text{RPC}} <$ 50 Pa and $\Delta p_{\text{TES1}} <$ 5000 Pa respectively, much smaller compared to $\Delta p_{\text{tot}} \geq$ 101325 Pa, leading to the conclusion that the main pressure drop occurred along the piping fittings and bends, valve orifices, and abrupt diameter changes. The RPC was observed to degrade due to the extreme rapid cooling rates of up to 101 °C min^{-1} but this degradation may be alleviated to some degree by the infiltration method to improve the RPC mechanical stability [4].

As aforementioned, the charging temperature into the TES 1 unit was below $T_{\text{ox,end}}$, too low for applying a heat recuperation step, caused by the conduction heat losses in the high-temperature piping between the reactor outlet and the TES HS flange (see Fig. 4), and resulting in a temperature drop of up to 1000 °C during the heat extraction step and for roughly 80% of the extracted energy being lost. These losses are expected to be reduced for large-scale DHS systems because of decreasing surface/volume ratio of the pipes.

Since no heat recuperation could be performed experimentally, the recovered heat Q_{recover} was evaluated theoretically by applying a TES storage efficiency on the measured extracted heat Q_{extract} ($Q_{\text{recover}} = \eta_{\text{TES}} Q_{\text{extract}}$). The calculated maximum $\eta_{\text{solar-to-fuel,max}}$ uses the reduced solar energy assuming Q_{recover} is utilized as $Q_{\text{solar}} = Q_{\text{solar,without HR}} - Q_{\text{recover}}$.

Multiple solar reactors may be used simultaneously to better utilize the solar energy input: while one solar reactor is on-sun during the reduction step, the others solar reactors are off-sun during the other 3 steps [2,7,28]. This concept was demonstrated recently with two solar reactors mounted on a solar dish concentrator by using a secondary reflector to direct the solar beam alternately between the two solar reactors during the reduction or oxidation steps [2]. In principle, heat recuperation could be performed directly from the solar reactor that finished reduction to the solar reactor that finished oxidation, thus eliminating the need for an intermediate TES unit.

A parametric study of the HTF flow rate was conducted, varying it from 50 to 90 L min^{-1} (Table 2). Fig. 8 shows the HTF temperature at the reactor outlet $T_{\text{heat extraction}}$ and the heat extraction effectiveness $\epsilon_{\text{heat extraction}}$ vs. the HTF flow rate $\dot{V}_{\text{HTF}}$. Under these conditions, $T_{\text{heat extraction}}$ during the heat extraction step was 1267 °C (Fig. 8, blue dashed line). Since no heat recuperation was performed, the N_2 inlet temperature during the heat extraction was always at ambient temperature. Thus, the system could potentially be simplified by removing TES 2, discarding recovery of the waste heat in the HTF after heat recuperation for the purpose of HTF preheating prior to heat extraction. Such a simplification can open new possibilities for the system design by removing piping and HTVs, decreasing the complexity and heat losses. Fig. 8 also presents the $\epsilon_{\text{heat extraction}}$ (dotted red line) for the different flow rates, which increases with $\dot{V}_{\text{HTF}}$ and reached a maximum value of 70%.

To better estimate the potential of the DHS concept for larger systems, which have a better surface-to-volume ratio, a dimensional analysis was performed for the 50 kW solar reactor of the EU-project Sun-to-Liquid, whose performance data is available [7] and whose design is similar to the 4 kW solar reactor used in this study. The various energy terms have been calculated for the 50 kW solar reactor using the measured values and multiplied by the characteristic dimensional factor $Q_{\text{i,S}} = f_{\text{sc}} Q_{\text{i}}$ (details in S.I.), and validated using the experimental values measured [7]. The portion of Q_{solar} that is used to heat the RPC increases from 27% for the 4 kW solar reactor to 42% for the 50 kW solar reactor. Thus, recovery of the sensible heat is crucial as the system is scaled-up.

Fig. 9 shows the energy balance during the heat extraction step, both for the lab-scale 4 kW solar reactor (Fig. 9(a)) and the scaled-up 50 kW reactor (Fig. 9(b)). For the 4 kW reactor, only about 2/3 of the total energy that exits the reactor during heat extraction is being transferred into the HTF. The remaining 1/3 is lost by re-radiation through the aperture (10%), and by conduction through the thermal insulation (23%). The re-radiation losses could be partially mitigated by using an HTF with high IR absorptivity [29]. For the 50 kW reactor,

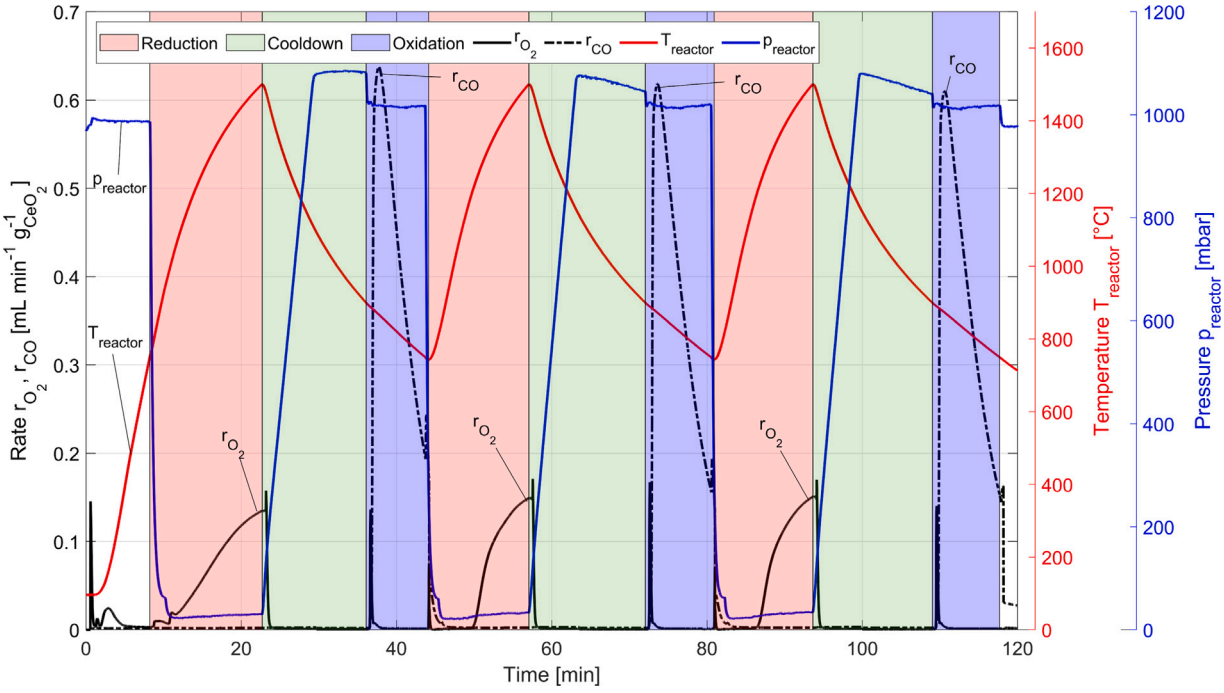

Fig. 6. Temporal variation of the nominal solar reactor temperature, reactor pressure, and specific O_2 and CO evolution rates for a reference run of three consecutive CO_2-splitting cycles with only reduction and oxidation steps but skipping the heat extraction and heat recuperation steps. Operation conditions: reduction step at $p_{reactor}$ = 22 mbar, $\dot{V}_{Ar}$ = 0.5 L min^{-1}, P_{solar} = 4.2 kW, T_{red} = 1500 °C; oxidation at: $p_{reactor}$ = 980 mbar, $T_{ox,start}$ = 900 °C, $T_{ox,end}$ = 750 °C, $\dot{V}_{CO_2}$ = 7 L min^{-1}. During the reactor cool-down step, the reactor was filled with CO_2 until $p_{reactor}$ = 1100 mbar.

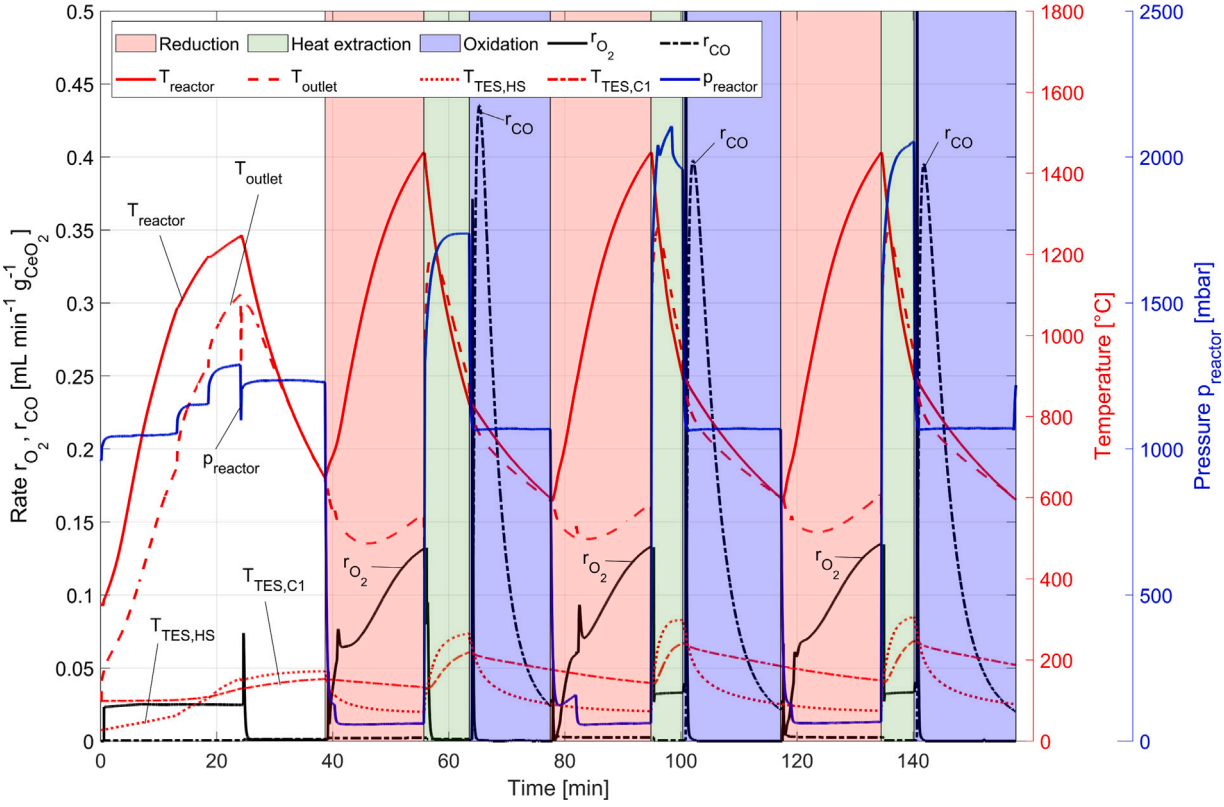

Fig. 7. Temporal variation of the nominal solar reactor temperature, reactor pressure, and specific O_2 and CO evolution rates for a representative run with 3 consecutive CO_2-splitting cycles of the DHS system. Only three steps were applied: reduction, heat extraction, and oxidation, but the heat recuperation step was skipped. Also plotted are the fluid temperature at the reactor outlet T_{outlet} (N_2 during heat extraction, CO and CO_2 during oxidation), the HTF temperature at the TES HS side (inlet during heat extraction), $T_{TES,HS}$, and the packed bed temperature $T_{TES,C1}$ (upper TC). Indicated are the preheating (white area), reduction (red area), heat extraction (green area), and oxidation (blue area) steps. Operation conditions: reduction at T_{red} = 1450 °C and $p_{reactor}$ = 56 mbar; heat extraction at $\dot{V}_{HTF}$ = 80 – 90 L min^{-1}; oxidation started at $T_{ox,start}$ = 900 °C until $T_{ox,end}$ = 600 °C.

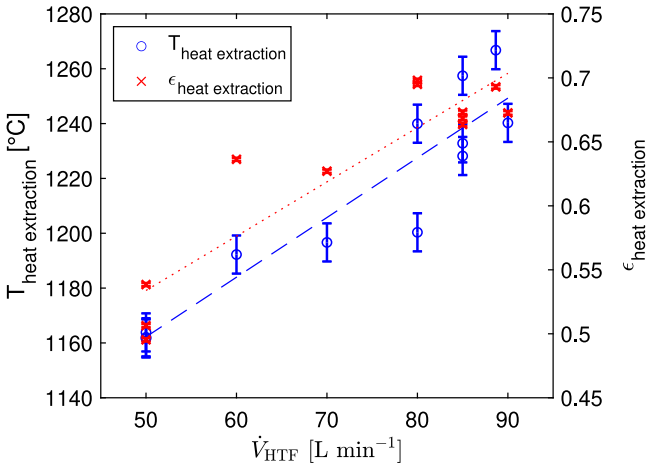

Fig. 8. Heat extraction temperature (blue) and heat extraction effectiveness (red) vs. the HTF flow rate for the DHS system. The points represent the measured values; the lines represent linear curve fitting. The reduction end temperature T_{red} was 1450 °C–1500 °C, the oxidation start temperature $T_{ox,start}$ was 875 °C–900 °C, and the oxidation end temperature $T_{ox,end}$ was 600 °C–650 °C. The reactor pressure $p_{reactor}$ was 55 mbar–61 mbar.

re-radiation losses remain at 10% but the conduction losses through the thermal insulation are significantly reduced to less than 8% due to improved volume-to-surface ratio. Adding thermal insulation might further decrease this value, but at the expense of increasing the required time to reach a steady cyclic behavior due to the larger thermal mass. The portion of the energy extracted from the reactor that is used to heat the HTF is 82%, and the predicted $\eta_{solar\text{-}to\text{-}fuel}$ is 9.82% (using η_{TES} = 1), almost twice than that without heat recovery. With η_{TES} = 0.75 (conservative estimate of the expected higher storage efficiency of a larger TES unit [27,30]), the calculated $\eta_{solar\text{-}to\text{-}fuel}$ is 7.97%, an increase of 51%.

The effect of heat recovery on the $\eta_{solar\text{-}to\text{-}fuel}$ is dependent on the overall performance of the solar reactor, and on how much energy is lost due to transient cooling and heating effects. In order to evaluate it, Eqs. (4) and (8) are used. Two cases are analyzed: (a) neglecting the transient heating/cooling losses $e_{transient}$ (assuming either they are also recovered, or that the insulation is sufficient to minimize these losses once the system reaches its steady cyclic operation); and (b) assuming the transient heating/cooling losses are proportional to the RPC sensible heating. For case (b), a value of $e_{transient} = 0.5e_{RPC,s}$ was selected, which is about half of the actual losses from the 50 kW reactor and five times smaller than the losses for the 4 kW solar reactor. This value was selected to reflect an increase in scale and/or improvement in the solar reactor design. The analysis was performed for the 50 kW solar reactor and for a baseline cycle with reduction at T_{red} = 1500 °C and p_{O_2} = 1 mbar and oxidation at T_{ox} = 900 °C and p_{CO_2} = 1 bar. The energy breakdown as a function of $\varepsilon_{heat\ recovery}$ is presented in Fig. 10a and b for the cases (a) and (b) respectively. For case (a) and without heat recovery ($\varepsilon_{heat\ recovery}$ = 0), $\eta_{solar\text{-}to\text{-}fuel}$ = 8.92%, a value which is slightly higher than those obtained in previous experimental work [7]. The differences are due to neglecting the transient losses ($e_{transient}$ = 0), the assumption that the complete redox material reaches uniform temperature (and thus fully reduced everywhere), the assumption that oxidation is performed isothermally and without losses, and the relatively low O_2 partial pressure. For this case, and further assuming a perfect heat recovery ($\varepsilon_{heat\ recovery}$ = 1), a value of $\eta_{solar\text{-}to\text{-}fuel}$ = 41.9% is obtained as the upper theoretical limit. The losses due to the exothermic nature of the oxidation reaction are becoming the dominant term limiting the efficiency in this case (28.3% of e_{total}), with the re-radiation losses as the second largest term (16.1%). For case (b) which includes the transient losses, $\eta_{solar\text{-}to\text{-}fuel}$ is 6.4% and 14.7%, without heat recovery ($\varepsilon_{heat\ recovery}$ = 0) and with full heat recovery ($\varepsilon_{heat\ recovery}$ = 1), respectively. It is noteworthy that the exothermic losses are reduced to 9.94% of e_{total} for full heat recovery, while the re-radiation losses slightly increase to 17.8% of e_{total}. The largest energy term in this case is $e_{transient}$, accounting for 52.8% of e_{total}. The improvement in $\eta_{solar\text{-}to\text{-}fuel}$ from $\varepsilon_{heat\ recovery}$ = 0 to $\varepsilon_{heat\ recovery}$ = 1 is more than double when $e_{transient}$ is nonzero. Recovering the transient losses is also possible, but might be counter-productive, as it will significantly increase the required energy flow during the heat extraction and recuperation steps, leading to long cycle times. This would lead to low utilization of the sunlight during the day, or the requirement for many solar reactors on a single concentrating system.

This result clearly shows that heat recovery is a critical key for improving the system performance, and that it is strongly coupled to the other losses of the reactor, mainly the transient heating/cooling losses. Minimizing them, which occurs naturally with increased size due to the more favorable volume-to-surface ratio, can significantly improve the $\eta_{solar\text{-}to\text{-}fuel}$ towards the values needed for commercial viability of this technology, currently estimated at 20% [2]. Moreover, $e_{transient}$ has a stronger effect during the first cycles, when the system is cold, and could also be mitigated by coupling the system with larger TES units for continuous operation.

The economic viability of solar-driven processes is strongly coupled to $\eta_{solar\text{-}to\text{-}fuel}$ because of the dominant investment costs of the solar concentrating infrastructure [2,31,32]. The higher $\eta_{solar\text{-}to\text{-}fuel}$ becomes the smaller the heliostat field for a given solar input, and consequently the lower the investments costs of the solar concentrating infrastructure. Thus, implementing heat recovery can significantly boost the value of $\eta_{solar\text{-}to\text{-}fuel}$ and consequently, improve the economics. In regards to estimated costs of the additional TES units in commercial applications, cheaper insulation materials, such as firebricks, can be used in lieu of the alumina–silica currently used. All other materials are relatively cheap and abundant. Further, closed-flow N_2 loop can be incorporated to prevent loss of HTF. Detailed techno-economic analyses are given in [32].

5. Conclusions

The experimental demonstration of the DHS concept was performed with multiple cycles consisting of the reduction, heat extraction, and oxidation steps under concentrated solar radiation. Up to 70% sensible heat at 1267 °C was extracted from the RPC of a 4 kW solar reactor. Energy flow simulations based on measured values of a 50 kW solar reactor predicts an upper limit of $\eta_{solar\text{-}to\text{-}fuel}$ = 42% for perfect heat recovery and without transient losses, and 14.7% with such losses included. High-temperature flow control still remains a challenge. The heat recovery step was not applied experimentally because the charging temperature in the TES was below the oxidation temperature due to significant heat losses through the piping. Obviously, long piping must be avoided. HTVs were shown to be feasible but at the expense of significant heat losses. Alternatively, valves at the cold sides of the TES could be implemented provided the volume to be evacuated during reduction would include both the solar reactor and the TES. The direct contact between HTF and the redox material provides efficient heat transfer but limits the application to inert fluids. Alternatively, an indirect heat exchanger could be developed and integrated in the solar reactor to perform the heat extraction and recovery without direct contact between the redox material and the HTF.

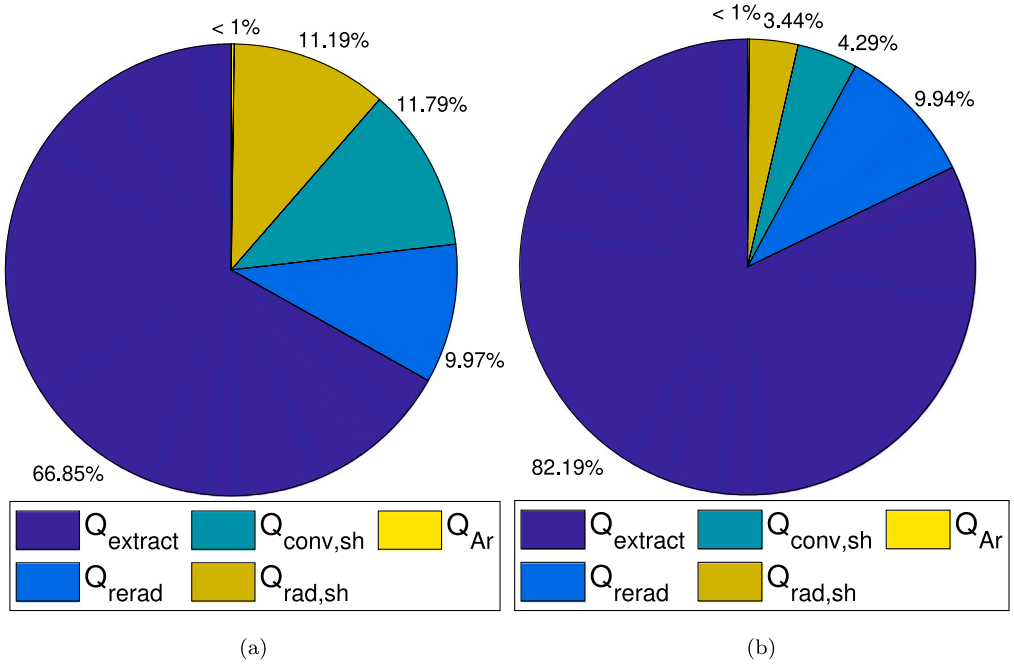

Fig. 9. Energy balance on the solar reactor during heat extraction for: (a) the 4 kW solar reactor, and (b) scaled-up 50 kW solar reactor.

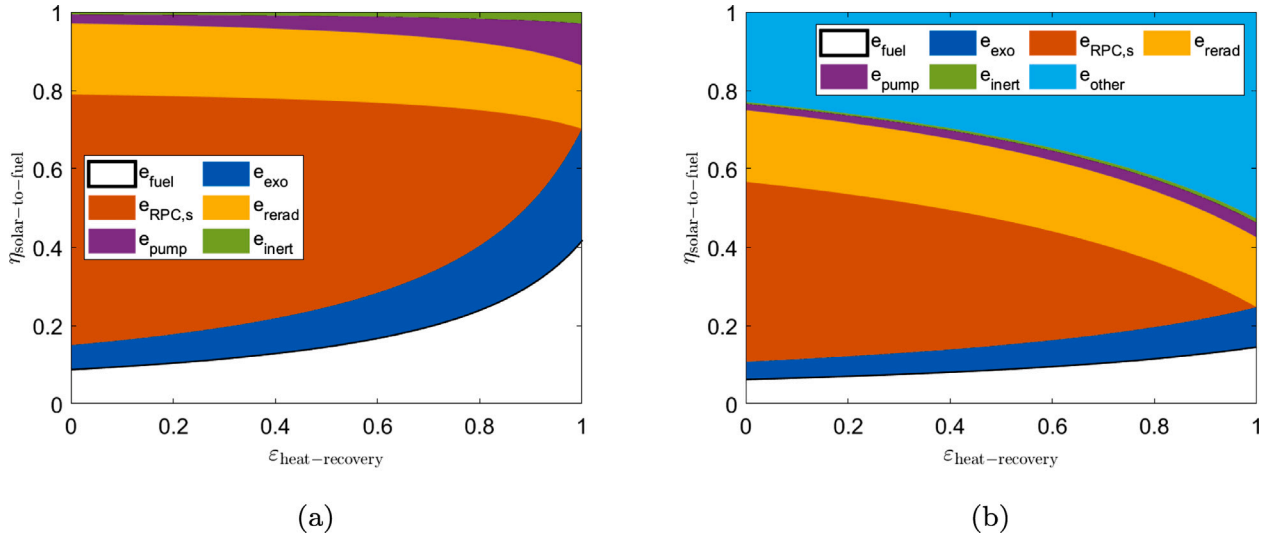

Fig. 10. Solar-to-fuel energy efficiency and energy breakdown as a function of the heat recovery effectiveness $\epsilon_{\text{heat recovery}}$ for: (a) $e_{\text{transient}} = 0$, and (b) $e_{\text{transient}} = 0.5e_{\text{RPC,s}}$. The analysis performed for the 50 kW solar reactor and for a baseline cycle with $T_{\text{red}} = 1500$ °C, $p_{O_2} = 1$ mbar, $T_{\text{ox}} = 900$ °C, and $p_{CO_2} = 1$ bar.

CRediT authorship contribution statement

Alon Lidor: Project conceptualization, Methodology, Investigation, Data processing, Manuscript writing, Supervision, Project management, Funding acquisition. **Yves Aschwanden:** Investigation, Data processing. **Jamina Häseli:** Investigation, Data processing. **Pit Reckinger:** Investigation, Data processing. **Philipp Haueter:** Engineering. **Aldo Steinfeld:** Project conceptualization, Manuscript writing, Supervision.

Declaration of competing interest

One or more of the authors of this paper have disclosed potential or pertinent conflicts of interest, which may include receipt of payment, either direct or indirect, institutional support, or association with an entity in the biomedical field which may be perceived to have potential conflict of interest with this work. For full disclosure statements refer to https://doi.org/10.1016/j.apenergy.2022.120211. Alon Lidor reports financial support was provided by European Union.

Data availability

Data will be made available on request.

Acknowledgments

This project has received funding from the European Union's Horizon 2020 research and innovation programme under the Marie Sklodowska-Curie grant agreement No 832535 (ECLIPSE). We acknowledge Julian Urech for his technical support and Lukas Geissbühler for a valuable discussion.

Appendix A. Supplementary data

Supplementary material related to this article can be found online at https://doi.org/10.1016/j.apenergy.2022.120211.

References

[1] Romero M, Steinfeld A. Concentrating solar thermal power and thermochemical fuels. Energy Environ Sci 2012;5(11):9234–45. http://dx.doi.org/10.1039/c2ee21275g.

[2] Schäppi R, Rutz D, Dähler F, Muroyama A, Haueter P, Lilliestam J, et al. Drop-in fuels from sunlight and air. Nature 2021;601(7891):1–6. http://dx.doi.org/10.1038/s41586-021-04174-y.

[3] Romero M, González-Aguilar J, Sizmann A, Batteiger V, Falter C, Steinfeld A, et al. Solar-driven thermochemical production of sustainable liquid fuels from H_2O and CO_2 in a heliostat field. In: Proceedings of the ISES solar world congress 2019. Freiburg, Germany: International Solar Energy Society; 2019, p. 1–12. http://dx.doi.org/10.18086/swc.2019.23.02.

[4] Marxer D, Furler P, Takacs M, Steinfeld A. Solar thermochemical splitting of CO_2 into separate streams of CO and O_2 with high selectivity, stability, conversion, and efficiency. Energy Environ Sci 2017;10(5):1142–9. http://dx.doi.org/10.1039/C6EE03776C.

[5] Lidor A, Fend T, Roeb M, Sattler C. Parametric investigation of a volumetric solar receiver-reactor. Sol Energy 2020;204(July 2020):256–69. http://dx.doi.org/10.1016/j.solener.2020.04.045.

[6] Lidor A, Fend T, Roeb M, Sattler C. High performance solar receiver–reactor for hydrogen generation. Renew Energy 2021;179:1217–32. http://dx.doi.org/10.1016/j.renene.2021.07.089.

[7] Zoller S, Koepf E, Nizamian D, Stephan M, Patané A, Haueter P, et al. A solar tower fuel plant for the thermochemical production of kerosene from H_2O and CO_2. Joule 2022;6:1606–16. http://dx.doi.org/10.1016/j.joule.2022.06.012.

[8] Scheffe JR, Steinfeld A. Thermodynamic analysis of cerium-based oxides for solar thermochemical fuel production. Energy Fuels 2012;26(3):1928–36. http://dx.doi.org/10.1021/ef201875v.

[9] Bulfin B, Call F, Lange M, Lübben O, Sattler C, Pitz-Paal R, et al. Thermodynamics of CeO_2 thermochemical fuel production. Energy Fuels 2015;29(2):1001–9. http://dx.doi.org/10.1021/ef5019912.

[10] Lapp J, Davidson JH, Lipiński W. Efficiency of two-step solar thermochemical non-stoichiometric redox cycles with heat recovery. Energy 2012;37(1):591–600. http://dx.doi.org/10.1016/j.energy.2011.10.045.

[11] Diver RB, Miller JE, Allendorf MD, Siegel NP, Hogan RE. Solar thermochemical water-splitting ferrite-cycle heat engines. J Sol Energy Eng 2008;130(4):041001. http://dx.doi.org/10.1115/1.2969781.

[12] Diver RB, Miller JE, Siegel NP, Moss TA. Testing of a CR5 solar thermochemical heat engine prototype. In: ASME 2010 4th international conference on energy sustainability, vol. 2. ASMEDC; 2010, p. 97–104. http://dx.doi.org/10.1115/ES2010-90093.

[13] Lapp J, Davidson JH, Lipiński W. Heat transfer analysis of a solid-solid heat recuperation system for solar-driven nonstoichiometric redox cycles. J Sol Energy Eng 2013;135(3):031004. http://dx.doi.org/10.1115/1.4023357.

[14] Lapp J, Lipiński W. Transient three-dimensional heat transfer model of a solar thermochemical reactor for H_2O and CO_2 splitting via nonstoichiometric ceria redox cycling. J Sol Energy Eng 2014;136(3):031006. http://dx.doi.org/10.1115/1.4026465.

[15] Falter CP, Sizmann A, Pitz-Paal R. Modular reactor model for the solar thermochemical production of syngas incorporating counter-flow solid heat exchange. Sol Energy 2015;122:1296–308. http://dx.doi.org/10.1016/j.solener.2015.10.042.

[16] Siegrist S, von Storch H, Roeb M, Sattler C. Moving brick receiver–reactor: A solar thermochemical reactor and process design with a solid–solid heat exchanger and on-demand production of hydrogen and/or carbon monoxide. J Sol Energy Eng 2019;141(2):021009. http://dx.doi.org/10.1115/1.4042069.

[17] Felinks J, Brendelberger S, Roeb M, Sattler C, Pitz-Paal R. Heat recovery concept for thermochemical processes using a solid heat transfer medium. Appl Therm Eng 2014;73(1):1006–13. http://dx.doi.org/10.1016/j.applthermaleng.2014.08.036.

[18] Felinks J, Richter S, Lachmann B, Brendelberger S, Roeb M, Sattler C, et al. Particle-particle heat transfer coefficient in a binary packed bed of alumina and zirconia-ceria particles. Appl Therm Eng 2016;101:101–11. http://dx.doi.org/10.1016/j.applthermaleng.2016.01.066.

[19] Yuan C, Jarrett C, Chueh W, Kawajiri Y, Henry A. A new solar fuels reactor concept based on a liquid metal heat transfer fluid: Reactor design and efficiency estimation. Sol Energy 2015;122:547–61. http://dx.doi.org/10.1016/j.solener.2015.08.019.

[20] Brendelberger S, Holzemer-Zerhusen P, von Storch H, Sattler C. Performance assessment of a heat recovery system for monolithic receiver-reactors. J Sol Energy Eng 2019;141(2):021008. http://dx.doi.org/10.1115/1.4042241.

[21] Thanda VK, Fend T, Laaber D, Lidor A, von Storch H, Säck JP, et al. Experimental investigation of the applicability of a 250 kW ceria receiver/reactor for solar thermochemical hydrogen generation. Renew Energy 2022;198(August):389–98. http://dx.doi.org/10.1016/j.renene.2022.08.010.

[22] Geissbühler L. Thermocline thermal energy storage: Advances and applications to CSP, compressed air energy storage, and solar fuels (Ph.D. dissertation), ETH Zürich; 2017, p. 262.

[23] Hathaway BJ, Bala Chandran R, Gladen AC, Chase TR, Davidson JH. Demonstration of a solar reactor for carbon dioxide splitting via the isothermal ceria redox cycle and practical implications. Energy Fuels 2016;30(8):6654–61. http://dx.doi.org/10.1021/acs.energyfuels.6b01265.

[24] Hoskins AL, Millican SL, Czernik CE, Alshankiti I, Netter JC, Wendelin TJ, et al. Continuous on-sun solar thermochemical hydrogen production via an isothermal redox cycle. Appl Energy 2019;249(April):368–76. http://dx.doi.org/10.1016/j.apenergy.2019.04.169.

[25] Furler P, Scheffe J, Marxer D, Gorbar M, Bonk A, Vogt U, et al. Thermochemical CO_2 splitting via redox cycling of ceria reticulated foam structures with dual-scale porosities. Phys Chem Chem Phys 2014;16(22):10503–11. http://dx.doi.org/10.1039/c4cp01172d.

[26] Bulfin B, Miranda M, Steinfeld A. Performance indicators for benchmarking solar thermochemical fuel processes and reactors. Front Energy Res 2021;9(July):1–12. http://dx.doi.org/10.3389/fenrg.2021.677980.

[27] Klein P, Roos TH, Sheer TJ. Parametric analysis of a high temperature packed bed thermal storage design for a solar gas turbine. Sol Energy 2015;118:59–73. http://dx.doi.org/10.1016/j.solener.2015.05.008.

[28] Lorentzou S, Zygogianni A, Pagkoura C, Karagiannakis G, Konstandopoulos AG, Saeck JP, et al. HYDROSOL-PLANT: Structured redox reactors for H_2 production from solar thermochemical H_2O splitting. In: SolarPACES 2017: International conference on concentrating solar power and chemical energy systems. Santiago, Chile, 2018, 130010. http://dx.doi.org/10.1063/1.5067144.

[29] Ambrosetti G, Good P. A novel approach to high temperature solar receivers with an absorbing gas as heat transfer fluid and reduced radiative losses. Sol Energy 2019;183:521–31. http://dx.doi.org/10.1016/j.solener.2019.03.004.

[30] Geissbühler L, Kolman M, Zanganeh G, Haselbacher A, Steinfeld A. Analysis of industrial-scale high-temperature combined sensible/latent thermal energy storage. Appl Therm Eng 2016;101:657–68. http://dx.doi.org/10.1016/j.applthermaleng.2015.12.031.

[31] Kim J, Johnson TA, Miller JE, Stechel EB, Maravelias CT. Fuel production from CO_2 using solar-thermal energy: System level analysis. Energy Environ Sci 2012;5(9):8417. http://dx.doi.org/10.1039/c2ee21798h.

[32] Falter C, Valente A, Habersetzer A, Iribarren D, Dufour J. An integrated techno-economic, environmental and social assessment of the solar thermochemical fuel pathway. Sustain Energy Fuels 2020;4(8):3992–4002. http://dx.doi.org/10.1039/d0se00179a.